Journal of Mathematical Biology (2021) 83:55
https://doi.org/10.1007/s00285-021-01674-3

Mathematical Biology

Reaction-diffusion models for morphological patterning of hESCs

Prajakta Bedekar[1] · Ilya Timofeyev[1] · Aryeh Warmflash[2] · Misha Perepelitsa[1]

Received: 8 January 2021 / Revised: 4 July 2021 / Accepted: 8 September 2021 /
Published online: 2 November 2021

Abstract

In this paper we consider mathematical modeling of the dynamics of self-organized patterning of spatially confined human embryonic stem cells (hESCs) treated with BMP4 (gastruloids) described in recent experimental works (Warmflash in Nat Methods 11:847–854, 2014; Chhabra in PloS Biol 17: 3000498, 2019). In the first part of the paper we use the activator-inhibitor equations of Gierer and Meinhardt to identify 3 reaction-diffusion regimes for each of the three morphogenic proteins, BMP4, Wnt and Nodal, based on the characteristic features of the dynamic patterning. We identify appropriate boundary conditions which correspond to the experimental setup and perform numerical simulations of the reaction-diffusion (RD) systems, using the finite element approximation, to confirm that the RD systems in these regimes produce realistic dynamics of the protein concentrations. In the second part of the paper we use analytic tools to address the questions of the existence and stability of non-homogeneous steady states for the reaction-diffusion systems of the type considered in the first part of the paper.

Keywords Morphological patterning · Cell differentiation · Reaction-diffusion equations

Mathematics Subject Classification 35K57 · 92-08

I. Timofeyev, M. Perepelitsa: Author acknowledge the support from NSF Grant DMS-1903270.
A. Warmflash: Author acknowledges support from NSF Grant MCB-1553228, Simons Foundation Grant 511079, and Welch Foundation Grant C-2021.

✉ Misha Perepelitsa
mperepel@central.uh.edu

[1] Department of Mathematics, University of Houston, Houston, TX, United States

[2] Laboratory of Systems Stem Cell and Developmental Biology, Department of BioSciences, Rice University, Houston, TX, United States

1 Introduction

During embryonic development, patterns of cell fates are established under the control of diffusible molecules known as morphogens. Simultaneously, cells divide and tissues are reshaped so that the embryo also acquires its physical form. While some models consider these as separate processes, with cell fate patterning preceding physical morphogenesis, others treat both of these aspects, as well as possible interactions between them Glover et al. (2017), Mercker et al. (2013). In the mammalian embryo, it is clear that growth, cell fate patterning, and the assumption of form all occur simultaneously, and the complexity of this process, as well as the difficulty of observing it in utero, have made both experimental and theoretical studies challenging.

Recently, several labs have developed an alternative approach based on embryonic stem cells (ESCs) and several models have been developed in which ESCs in vitro mimic aspects of embryonic patterning reviewed in Fu et al. (2021), Liu and Warmflash (2021). In this study, we consider an experimental model in which human ESCs (hESCs) are grown in confined geometries and differentiated by application of the signaling factor BMP4 Warmflash et al. (2014), Etoc et al. (2016), Heemskerk et al. (2019), Chhabra et al. (2019). In this model, the cells are patterned into extraembryonic fates and the three embryonic germ layers, endoderm, mesoderm, and ectoderm, under the control of BMP, Wnt, and Nodal signals, the same set of pathways which pattern the mammalian embryo at this stage Arnold and Robertson (2009). This model represents a considerable simplification of the in vivo process as the hESC colony remains the same size and shape throughout the process so overall tissue growth and physical morphogenesis do not need to be considered. Moreover, cell tracking experiments have shown limited cell movements which cannot explain the cell fate patterning Chhabra et al. (2019), and therefore chemotactic processes can also be neglected when modeling these processes. Finally, while some mechanical influences on cell fate may be present Muncie et al. (2020) these appear to function by influencing the chemical signaling pathways, which are strictly required for pattern formation Fu et al. (2021), Etoc et al. (2016), Chhabra et al. (2019). Thus, in this paper we consider the process by which chemical signaling pathways pattern hESC colonies but do not treat physical morphogenesis, chemotaxis, or the influence of mechanical signaling as these are limited or not present in the experimental system under consideration.

The use of reaction-diffusion (RD) systems to model the evolution of chemical patterning in the developing organism started with the seminal work of Turing (1952), who observed that in some cases the homogeneous distributions of chemicals with coupled reaction rates are not stable, and upon small perturbations give rise to sizable, non-homogeneous patterns of chemicals. Cells at the peaks of these patterns can then differ from the remainder of the cells in their cell fates, growth rates, or morphogenetic movements. That is, the morphological patterning is a consequence of prior chemical "pre-patterning."

This approach have been extensively developed over the years, see for example Koch and Meinhardt (1994), Gierer and Meinhardt (1972), Raspopovic et al. (2014), Nakamura et al. (2006), Glover et al. (2017). This framework has been extended various settings including time-dependent domains due to growth of cells, Crampin et al. (1999) and Van Gorder et al. (2021). Other mechanisms of morphogenesis such

as of mechanical, mechanochemical and chemotaxis types had been developed, see for example Murray et al. (1983), Murray (1989), Mercker et al. (2013), Brinkmann et al. (2018), Maini et al. (2006), Hillen and Painter (2009).

These models take into account not only chemical but also mechanical properties of treated cell samples, such as, for example, the motion of chemical in the sample induced by the growth of cells. However, as noted above, such effects can be neglected in the specific experimental system that we are modeling, and so we confine our approach here to RD models of chemical systems.

In this paper we will discuss the patterning of hESC colonies based on the recent experimental findings by Warmflash et al. (2014), Chhabra et al. (2019) and Heemskerk et al. (2019). In a typical experiment, a spatially confined colony of cells is treated with BMP4 (bone morphogenetic proteins) which leads to differentiation of cells into the three embryonic germ layers: endoderm, mesoderm, and ectoderm, surrounded by an outer ring of extraembryonic cells. Collectively, these studies have shown that this process does not fit into the Turing paradigm of patterning, or into the other mechanisms mentioned above.

It has been established in earlier works, see for example Arnold and Robertson (2009), that BMP4 results in expression of Wnt and Nodal proteins that are essential for formation of germ layers.

The evidence accumulated in Chhabra et al. (2019) indicates that fate differentiation occurs not after the formation of stable patterns of BMP4/Wnt/Nodal, but concurrently, during the propagation of signaling waves of Wnt and Nodal, while the Turing-type process assumes that chemical gradients form and the information in these is then used to drive cell fate patterning. Additionally, the terminal, stable distributions of these proteins do not correspond (decisively) to the location of the germ layers. For example, Wnt and Nodal signaling, which synergize to generate mesendoderm, both spread into the middle region where ectoderm forms. We mention in passing, that the distributions of proteins do tend to non-homogeneous, almost radial, steady states. Moreover, as noted above, Chhabra et al. (2019) performed a series of experiments ruling out the cell motion and cell growth as effective mechanisms of morphogenesis. The later facts points strongly in favor of a RD system as the correct mathematical model.

We summarize below some of the characteristic features for the dynamics of distribution of proteins during the patterning, obtained in Chhabra et al. (2019) and Heemskerk et al. Heemskerk et al. (2019), that we address in this paper.

(1) Initially high and uniform over the entire domain, BMP4 signaling activity evolves into a region of high activity near the boundary and low activity in the middle and central parts of the domain;
(2) BMP4 activity at the boundary initiates waves of Nodal and Wnt that move into the interior towards the center of the domain;
(3) propagation of the Nodal wave proceeds independently of BMP4 (and Wnt), after a certain activation period;
(4) distributions of BMP4, Wnt and Nodal activities tend to steady states, by the end of the experiment, with the peaks at the boundary, middle of the domain and the center of the domain, respectively. The difference between the peak value of Wnt

and its value at the center is smaller than the difference between the peak value and the values near the boundary. The final distributions of all proteins appear to be radial, non-homogeneous steady states.

While the understanding of all mechanisms is far from being complete, an effort was made to generate dynamics consistent with (1)–(4) in the framework of activator-inhibitor RD systems. Tewary et al. (2017) developed a RD model model that produces realistic patterns of BMP4, with realistic dependence on parameters, such as the size of the cell colony. However, due the fact that the reaction part of the model is linear, the model requires selection of *matching* boundary and initial conditions, that do not reflect the state of the problem at the beginning of the experiment. For example, it was assumed that BMP4 inhibitor does not diffuse from the sample boundary, and, initially, peaks at the center of the sample. Thus, the model is partially "exogenous".

Chhabra et al. (2019) addressed the mathematical modeling of dynamics described in part (3) of the above list. In this model, BMP4 acts as an activator for Wnt, which in its turn activates Nodal. The key assumption is a reaction term in the equation for Nodal, that incorporates a threshold parameter, depending on the concentration of Nodal, that switches production from being Wnt dependent to auto-catalytic. Other assumptions include structurally different mechanisms of activation/inhibition for Wnt and Nodal.

The analysis of RD systems in the above mentioned papers relies on the numerical solutions of the corresponding systems of PDEs.

The purpose of the present paper is to develop closed form models based on the classical Gierer-Meinhardt activator-inhibitor system, see Eqs. (4) and (5) below, that reproduce behaviors (1)-(4). By the closed form we mean, a solution to an initial-boundary value problem where the initial and boundary conditions reflect the actual experimental setup.

In particular, we assume that all substances can diffuse off the colony edge, and use "Newton's law of cooling" with appropriate background values of the substances.

In the first part of the paper, using numerical simulations, we show that realistic dynamics of the proteins can be obtained by choosing suitable reaction coefficients in a activator-inhibitor system. The dynamics of BMP4 is best described by a system with a single, stable node, to which we will refer as type 1 system, see Sect. 2. The dynamics of Wnt and Nodal systems fit to the patterns produced by type 2 systems, which have a stable node, a stable focus and a saddle point in the phase plane. Moreover, we show that different behaviors of Wnt and Nodal, as described in (5), can be attributed to the size of the reaction coefficients alone. This is due to a general fact that scaling reaction coefficients in a RD systems, which leaves the phase portrait unchanged, while retaining the same diffusion coefficient, results in a different dynamics and, in particular, in different steady states. Thus, we provide another explanation of phenomenological properties (1)–(4) based on the dynamical differences between structurally similar systems of PDEs. The analysis can be useful in obtaining estimates of the ranges of the reaction coefficients that distinguish BMP4, Wnt and Nodal at the level of activator-inhibitor systems.

In the second part of the paper we address the stability property in part (4). The main mathematical difficulty comes from the fact that the RD models (equations

+ boundary conditions) in question do not have, in general, homogeneous steady states. Thus, linearizing equations on a constant state, and solving for eigenvalues and eigenfunctions does not provide meaningful information, because the constant states are not solutions, the fact that sometimes is overlooked in biological literature. The growth of oscillations should be measured with respect to a proper steady state, which, in this case is non-homogeneous.

This leads us to the following problems that we address in this paper: (a) determining if solutions asymptotically converge to a steady state, and (b) finding conditions under which such steady states are stable.

There are local in time, unique, classical solutions to RD systems in the Hólder space $C^{2+\alpha,1+\alpha/2}$, as was proved by Ladyzenskaja et al. (1995) for a more general system of parabolic equations. Estimates on the *max* norm of the solution are needed to extend solutions for all times $t > 0$. This was done by Rothe (1984) for activator-inhibitor systems with zero Neumann boundary conditions, which does not apply in our case. Moreover, the estimates obtained in Rothe (1984) depend on the diffusion coefficients, which greatly complicates the asymptotic analysis. We note here, that the special structure of the activator-inhibitor equations does not allow the application of the theory of invariant regions of Chueh et al. (1977), another well-known technique for the asymptotic analysis, see for example a book of Smoller (1983).

Our approach is to rely on the maximum principle for the parabolic equations to obtain the uniform in (x, t) estimates of the solution. The application of this method places some restrictions on the coefficients of the RD system. The key point here is that the bounds are independent of the diffusion coefficient.

Then, we use the energy-types estimates for L^2 norms of the solution and its time derivative to identify a suitable stability condition that implies the exponential decay of the norm of the time derivative. Further analysis required to bound the spatial gradient of the solution in L^2 norm, with an upper bound, independent of time. The later fact allows us to extract a strongly convergent sequence $\mathbf{u}(x, t_n)$ with $t_n \to \infty$, whose limiting point is a steady state solution of the activator-inhibitor system. Here, $\mathbf{u}$ is a solution vector $\mathbf{u} = (u, v)$. Finally we show that such steady state, $\mathbf{u}_s$, is the limit of the $\mathbf{u}(x, t)$, at $t \to \infty$. The stability condition mentioned above, for given source terms $f(x)$, $g(x)$, size of the domain Ω and the diffusion coefficient μ restricts the size of the initial data $\max_\Omega |\mathbf{u}_0|$. This condition defines the basin of attraction for the steady state, i.e., there is a ball B in L^∞, centered at zero, such the steady state $\mathbf{u}_s$ belongs to B and for any initial data $\mathbf{u}_0 \in L^\infty \cap C^{2+\alpha}$, solution $\mathbf{u}(x, t)$ converges to that steady state.

2 RD models of activator-inhibitor type

We consider an activator-inhibitor RD system

$$\partial_t u - \mu_u \Delta u = -au + \frac{bu^2}{1+v}, \tag{1}$$

$$\partial_t v - \mu_v \Delta v = -cv + du^2, \tag{2}$$

where μ_u, μ_v are positive diffusion coefficients, $a, c > 0$ are rates of decay and b, d are positive reaction coefficients. This system was introduced by Gierer and Meinhardt (1972). The inhibitor enters the first equation through the factor $(1 + v)^{-1}$, where we added 1 to avoid infinitely high rates when the level of the inhibitor v is small. This is a natural assumption in the experiments described in Warmflash et al. (2014), Chhabra et al. (2019).

Here we denote by $f(u, v)$ and $g(u, v)$ the right-hand side of Eqs. (1) and (2). There is a single fixed point (stable node) $(u_0, v_0) = (0, 0)$, if $b^2c < 4a^2d$. When $b^2c > 4a^2d$ there are three fixed points $(0, 0)$, (u_1, v_1), (u_2, v_2) where

$$u_{1,2} = \frac{cb \pm \sqrt{(cb)^2 - 4a^2cd}}{2da}, \quad v_{1,2} = \frac{b}{a}u - 1. \tag{3}$$

In this case $(0, 0)$ is a stable node, as the gradient matrix is

$$\frac{\partial(f, g)}{\partial(u, v)} = \begin{bmatrix} -a & 0 \\ 0 & -c \end{bmatrix}.$$

At other two points, the gradient matrix can be computed to be equal to

$$\frac{\partial(f, g)}{\partial(u, v)} = \begin{bmatrix} a & -\frac{a^2}{b} \\ 2du & -c \end{bmatrix},$$

where u is evaluated at a fixed point. Thus, we obtain the values of the trace and the determinant of the gradient matrix as

$$\text{trace} = a - c, \quad \text{Det} = \frac{2da^2}{b}u - ac,$$

These values determine the type of each fixed point. Substituting the values for $u_{1,2}$ from (3) we find that $\text{Det} = \pm\sqrt{(ac)^2 - 4dca^4b^{-2}}$. This gives a saddle point, when the value of the determinant is negative. The remaining point is either a stable focus $(a < c)$, a center $(a = c)$, or an unstable focus $(a > c)$. For the non-linear system (1), (2), the last two possibilities result in motion characterized by oscillations. This type of motion is not observed in the experiment discussed in this paper, so we assume that $a < c$. The null clines for different values of the decay/reaction coefficients are sketched in Fig. 1, which we use to distinguish the corresponding RD systems as type 1 and type 2.

We will use system (1), (2) to model the dynamics of BMP4 and its inhibitor Noggin. To study the signaling waves of Nodal and Wnt we will use a source term $f(x)$ in the activator equation that models the influence of BMP4 on production of Wnt:

$$\partial_t u - \mu_u \Delta u = -au + \frac{bu^2}{1 + v} + f(x), \tag{4}$$

$$\partial_t v - \mu_v \Delta v = -cv + du^2. \tag{5}$$

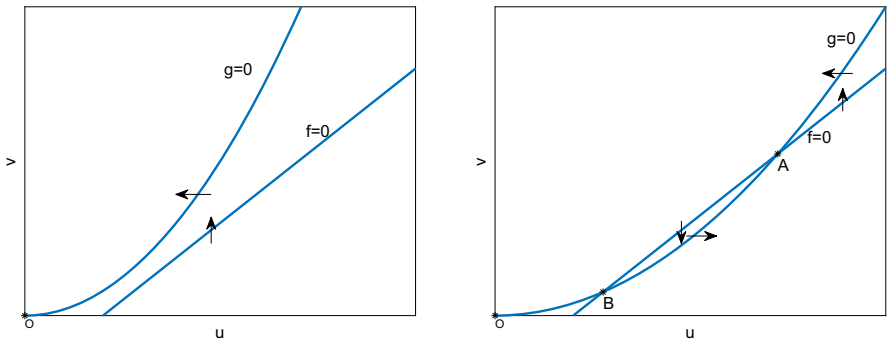

Fig. 1 Null clines for the reaction dynamics. Left plot is type 1 reaction with a single fixed point O (stable node). Right plot is type 2 reaction with a stable node O, sable focus A, and saddle B. Arrows show the direction of the flow field

Here u is the concentration of Wnt and v the its inhibitor DKK. In the numerical simulations we will assume that $f(x)$ is concentrated near the boundary of the domain which reflects the experimentally observed distribution of BMP. The activation of Nodal occurs through BMP $\rightarrow$ Wnt $\rightarrow$ Nodal signaling pathway. We will model this by a simplifying to BMP $\rightarrow$ Nodal signaling, and using Eqs. (4) and (5), with a different set of reaction coefficients, to model the dynamics of Nodal and its inhibitor Lefty.

As we will show in by numerical simulation, the system of BMP4 and its inhibitor has a better fit into the reaction system of type 1, see Fig. 1, while the systems for Wnt and Nodal are better described by type 2 dynamics.

The initial data correspond to the high initial concentration of BMP4 and low (zero) concentrations of other chemicals, in accordance with experiments described in Warmflash et al. (2014).

To complete the model, we need to postulate boundary conditions for chemical concentrations. It should be emphasized that the boundary conditions are the integral part of the solution, that plays an important part in the way the dynamics proceeds. According the experimental setup, the chemicals can diffuse from the domain of a cell sample, the intensity of this "leaking" being proportional to the difference between the boundary concentration of the chemical and the "background" concentration. For BMP4 it is reasonable to take the background concentration at the fixed level $\bar{u}$ that equals to the initial concentration of BMP4. For other chemicals in question, the background concentration is zero. This is so-called "Newton's law of cooling." It is expressed as

$$\frac{\partial u}{\partial n} = h_u(\bar{u} - u), \quad h_u > 0,$$

where n is the external, unit normal vector at $\partial\Omega$. Similarly, for the inhibitor,

$$\frac{\partial v}{\partial n} = -h_v v, \quad h_v > 0.$$

Table 1 Dimensionless reaction and diffusion parameters for the activator-inhibitor RD systems (1), (2) and (4), (5), used in numerical simulations

	bmp4/noggin	wnt/dkk	nodal/lefty
a	77.76	77.76	31.104
b	77.76	194.4	77.76
c	77.76	194.4	77.76
d	77.76	97.2	38.88
μ_u	3.8	3.8	3.8
μ_v	19	19	19
h_u	172.8	172.8	172.8
h_v	172.8	172.8	172.8

We note that an earlier works on mathematical modeling of hESC development such as Tewary et al. (2017), used *ad hoc* boundary conditions, not consistent with the experimental setting. An alternative way to deal with the boundary, is to embed the reaction domain into a larger domain where chemicals can only diffused, and postulate, for example, no-flux boundary conditions on the larger domain, as was done by in Chhabra et al. (2019). The reason being that, the precise form of the boundary conditions on the larger domain should have minimal effect on the domain where the reaction takes place. It should be noted here that this approach may lead to a different patterning on the reaction domain, see Krause et al. (2020).

3 Numerical simulations

Simulations are performed for RD systems written in scaled variables, using the values of coefficients of the magnitude typically occurred in experimental studies, see Appendix for details. In particular, the computational domain is a disk of radius 1, and time t is measured in days. The values of parameters for system (1), (2) for BMP4/Noggin, and system (4), (5) for Wnt/DKK and Nodal/Lefy, used in the simulations, are listed in Table 1.

The parameters are selected is such a way that RD system for BMP4 is of type 1, and the systems for Wnt and Nodal are of type 2. Reaction coefficients for Nodal system differ by a factor of 0.4 from the corresponding coefficients for Wnt system, which means that the phase portraits for the reaction dynamics are identical in both cases.

The source term $f(x)$ in (4) is set to be supported near the boundary of the disk:

$$f(x) = \begin{cases} 670 & |x| > 0.85, \\ 0 & |x| < 0.85. \end{cases}$$

Finally, the background state $\bar{u}$ is set to 3 for BMP4, as well as the initial values for BMP4. All other chemicals have zero initial values, and zero background states.

We will show below that behaviors 1.-4., listed in the Introduction, are captured by the RD models described here. The exact timing of different phenomena described

below does not necessarily correspond to experimentally observed values. That would require more precise estimation of the parameters of the model. Our main goal is to establish that qualitatively correct behavior is produced by the model.

3.1 Terminal concentrations of proteins

The numerical simulations show that concentrations of all three proteins approach radial, steady state profiles by $t = 1$ day. Figure 2 shows 2d and 3d plots of concentrations of the proteins at $t = 3$ days. BMP4 is concentrated at the boundary of the domain. Wnt peaks in the middle section, but takes comparable values at the center, and Nodal peaks at the center but somewhat extends to the middle section of the domain.

The appearance of steady states was identified when the change between the successive iterations of the numerical solution became less than 10^{-6} units, over a period of time of 1 day.

To illustrate the difference between three different diffusion-reaction regimes we map the radial cut of each protein and its inhibitor in the phase plane on Fig. 3. Point B indicates the values at the boundary of the disk and point C represents the values at the center. The plots also show the stable fixed point, S, for the corresponding reaction dynamics. BMP4 starts at non-zero value at the boundary due to the influence from non-zero background state $\bar{b}$ and then moves towards zero, according to the reaction, as one moves to the center of the disk. Point S is a stable focus for Wnt/DKK and Nodal/Lefty pairs, however the reaction coefficients are stronger in Wnt system than in Nodal system. This results in the radial profile of Wnt/DKK being "bent" in the direction of the reaction. This property results in maximum of Wnt to be located in the middle of the disk, whereas Nodal has maximum at the center.

3.2 Signaling waves of Wnt and Nodal

Figure 4 shows the evolution of concentrations of Wnt and Nodal as functions of time. In both cases, the concentration first increase near the boundary, where $f(x)$ is supported and then they move toward the center. This behavior corresponds to the "signaling waves" of the proteins described in Introduction.

3.3 Effect of inhibition of BMP4

Figure 5 shows the effect of inhibition of BMP4 at time indicated by the variable t_c on the shape of the final concentration at time $t = 3$ days. That is, term $f(x)$, describing the influence of BMP4 in (4), is set to zero for $t > t_c$.

The simulations show that there is a critical time t_0 with the property that if BMP4 is inhibited prior to t_0 the system converges to zero steady-state, but when BMP4 is inhibited after t_0 the system proceeds autonomously to a non-homogeneous, non-zero steady state. For Wnt dynamics t_0 is estimated to be between 0.001 and 0.005 days, and for Nodal, between 0.005 and 0.01 days, the difference is due to the difference in the magnitude of the reaction coefficients.

3.4 Dependence on parameters

For small variations of parameters given in Table 1 the numerical simulation produce qualitatively similar results, indicating that the problems are stable. That is, the terminal steady state concentrations are stable. This property is lost when the larger variations. We performed the numerical simulation of BMP/Noggin dynamics with large gap in diffusion coefficients, by selecting $\mu_u = 1\,\mu m^2/sec$ and $\mu_v = 55\,\mu m^2/sec$, (instead of $\mu_u = 11\,\mu m^2/sec$, and $\mu_v = 55\,\mu m^2/sec$ used previously), while keeping all other parameters.

Figure 6 shows 2d and 3d plots of non-radial profile of BMP4 at time $t = 3$ days. The non-radial perturbations start to develop from a radially symmetric profile at the time about $t = 0.2$ days. Note that, due to the radial symmetry of equations, the problems has a unique, classical, radially symmetric solution if the initial data have this property, but the numerical solution deviate from it significantly.

A possible explanation of this phenomenon is that the problem has an unstable radially symmetric steady state to which the system moves from its initial values. Small deviations from radially symmetry due the numerical approximation lead to the growth of perturbations shown on the figure. That is, this is the case of Turing instability.

Interestingly, the instabilities appear to be restricted to the boundary, and further simulations (not shown here) produce a different number of peaks, with further variations in the diffusion coefficients. This non-homogeneous profile might, in principle, be associated with the formation of the outer ring of germs in a cell colony. Further investigation of a coupled BMP4-Wnt-Nodal system is needed to clarify if this behavior bears some significance in actual biological processes.

4 Existence and stability of steady-state solutions

One of the main features of the models considered in this paper and experimental works cited in the introduction is the formation non-homogeneous steady-states of the chemical concentrations. Moreover, these steady-states appear to be stable, as none of the Turing-type instabilities are observed in the experimental setting, see Chhabra et al. (2019). In this section we address the question of existence of stable steady-state solutions. The results that we prove below, apply to RD systems in the form:

$$\partial_t u - \mu \Delta u = -au + \frac{bu^2}{1+v} + f(x), \tag{6}$$

$$\partial_t v - \mu \Delta v = -cv + du^2 + g(x), \tag{7}$$

with the Direchlet boundary conditions

$$u(x,t) = 0, \quad v(x,t) = 0, \quad (x,t) \in \partial\Omega \times [0, +\infty), \tag{8}$$

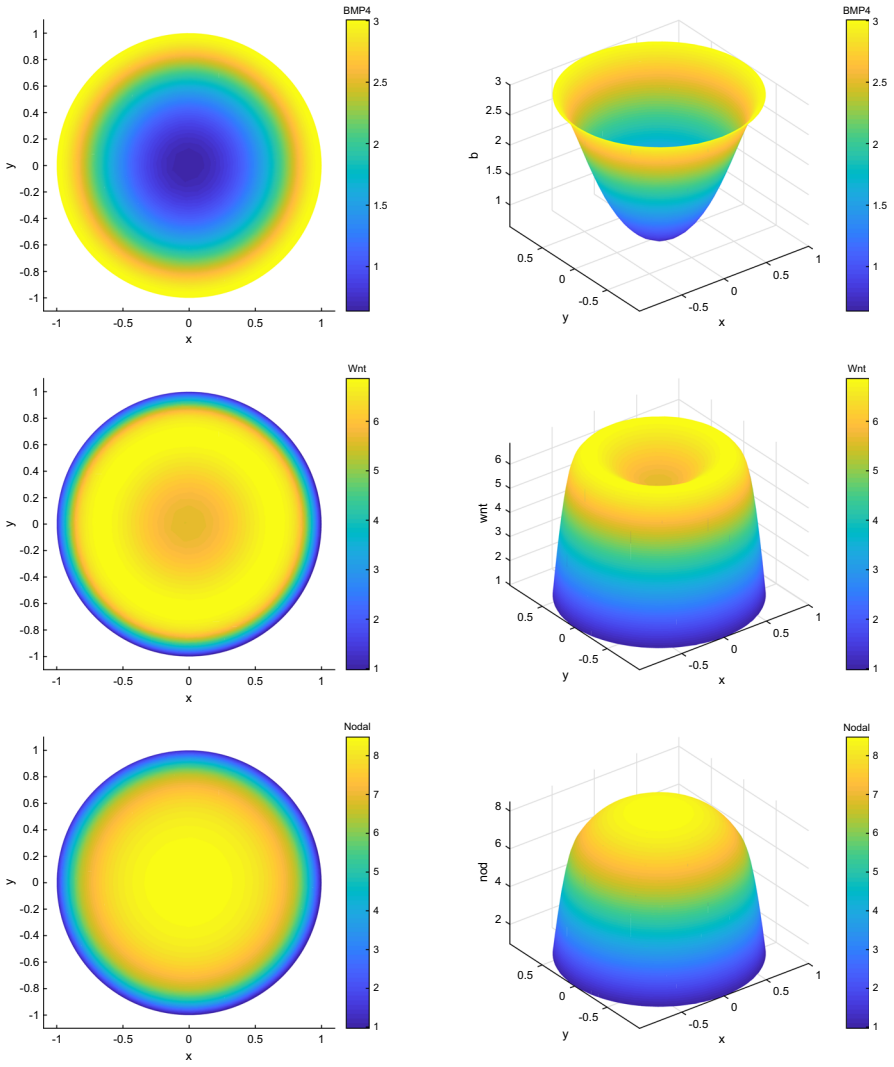

Fig. 2 Steady state concentrations of BMP4, Wnt and Nodal at time $t = 3$ days

and initial conditions

$$u(x, 0) = u_0(x), \quad v(x, 0) = v_0(x), \quad x \in \Omega. \tag{9}$$

The boundary conditions (8) can be seen as a limiting case of the boundary conditions from Sect. 2, when the rates of cooling h_u, $h_v \to +\infty$, i.e., there is high rate of transfer of chemicals to or from the background state. This simplification is due to certain limits of applicability of the analytical tools that we use in the proof of Theorem 1 below.

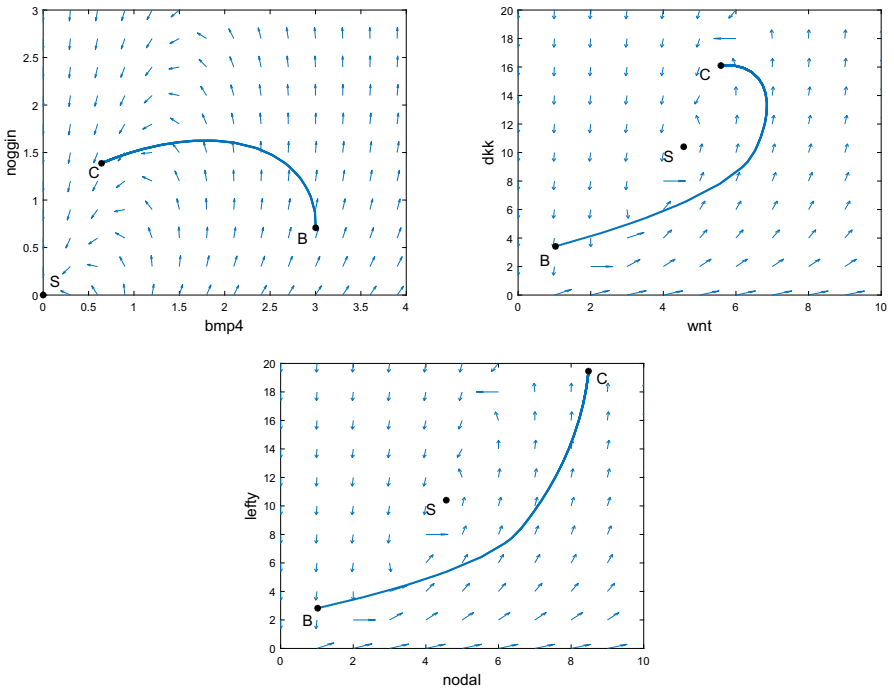

Fig. 3 Radial sections of three pairs of activator-inhibitors in the phase plane. The plots show the values of bmp4/noggin, wnt/dkk, and nodal/lefty from the boundary B to the center of the colony C, when the concentrations reach steady states, at $t = 3$ days. On the top plot, S is the stable node for the reaction dynamics. On the middle and bottom plots, S is a stable focus with counterclockwise rotation. Plots also show velocity fields of each reaction system

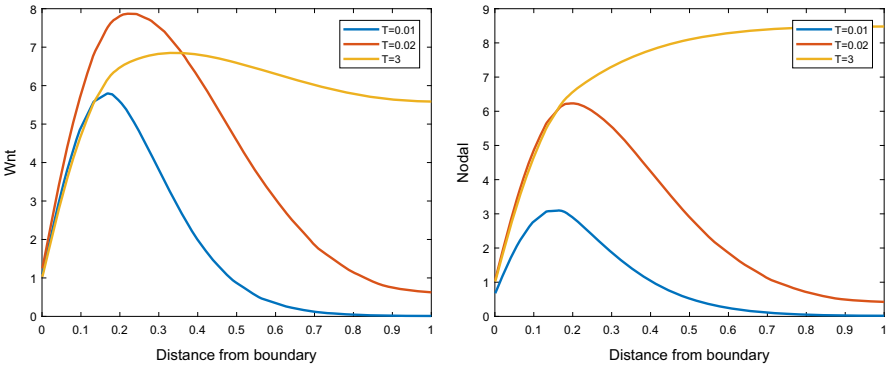

Fig. 4 Signaling waves of Wnt and Nodal. Plots represent radial profile of the proteins at increasing moments of time T. Initial concentrations are zeros for both proteins

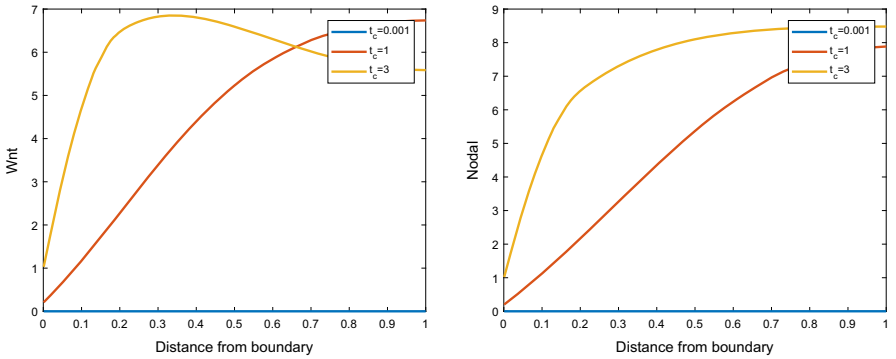

Fig. 5 Effect of BMP inhibition at time t_c on the terminal concentrations of Wnt and Nodal. Concentrations with $t_c = 3$ correspond to no inhibition of BMP4. Plots show switching from a zero steady state to a non-zero state, when the activation time of BMP4 exceeds certain threshold value, but it is inhibited afterwards

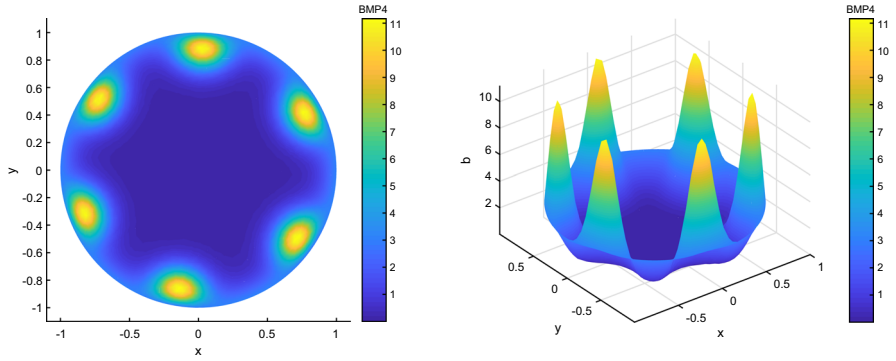

Fig. 6 Instabilities in BMP4/Noggin dynamics. The figure shows 2d and 3d plots of the result of the numerical simulation of concentration of BMP4 at $t = 3$ for the diffusion coefficients $\mu_{bmp} = 1$ and $\mu_{nog} = 55$ and the colony size of $500\mu m$

We would like to mention the well-known method of invariant regions by Chueh et al. (1977), for establishing time asymptotic behavior of solutions of reaction-diffusion systems does not apply to the present problem. The latter method applies to reaction-diffusion systems in the form

$$\frac{\partial u}{\partial t} - D\Delta u = F(u, t), \tag{10}$$

where $u \in \mathbb{R}^n$, $(x, t) \in \Omega \times [0, +\infty)$, D is $n \times n$, diagonal matrix with non-negative entries, and the vector source term $F \in \mathbb{R}^n$. The system is supplied with the zero-flux boundary conditions

$$\frac{\partial u}{\partial n} = 0, \quad (x, t) \in \partial\Omega \times [0, +\infty).$$

For the method to work the must have bounded invariant regions in order to establish bounds on supremum norm of $|u(x,t)|$. Next, the method relies on the fact that time asymptotic behavior of solutions of (10) can be compared with the solution of the system of ODEs:

$$\frac{du}{dt} = F(u,t),$$

meaning that the limiting behavior of (10) is a homogeneous (constant in x) state.

If we look at the system (6), (7), we see that the right-hand side explicitly depends on x through functions $f(x)$ and $g(x)$. The boundary conditions (8) differ as well. Thus, in general, the steady-states of the problem (6), (7) and (8) are non homogeneous (non-constant). Moreover, and this is a major obstacle, it can be shown that system (6)–(7) does not have invariant regions either, so that the uniform estimates must be obtained by other means.

4.1 Main theorem

We will use the standard notation for the spaces of continuous, Hölder continuous functions, as well as L^p spaces. For definitions, we refer readers to Ladyzenskaja et al. (1995). Norms in $L^p(\Omega)$ space will denoted by $\|u\|_p$, $1 \le p \le \infty$. We let $Q_T = \Omega \times (0,T)$ and $\Gamma_T = (\Omega \times \{t=0\}) \cup (\partial\Omega \times [0,T])$, for $T > 0$.

Now we state our main result, that we will be proved below.

Theorem 1 *Let Ω be an open, bounded, set with $C^{2+\alpha}$ boundary and $\alpha \in (0,1)$. Let $f(x), g(x) \in C^{\alpha}(\overline{\Omega})$ be non-negative functions, $u_0, v_0 \in C^{2+\alpha}(\overline{\Omega})$, $u_b, v_b \in C^{2+\alpha}(\partial\Omega)$, and necessary compatibility conditions between the initial and boundary values hold. Then, there exists a unique classical solution of (6)–(9) on $\Omega \times [0,\infty)$. Moreover, for any $T > 0$, $u, v \in C^{2+\alpha,1+\alpha/2}(Q_T)$ and the following properties hold.*

(1) *$u(x,t), v(x,t)$ are non-negative and bounded above with a constant independent of x, t, and μ.*
(2) *There is C_s – a polynomial in positive powers of $\|u_0\|_\infty$, $\|v_0\|_\infty$, $\|f\|_\infty$ and $\|g\|_\infty$, independent of μ, such that if inequality*

$$C_s < \mu C(\Omega), \tag{11}$$

holds, for a certain $C(\Omega) > 0$ depending only on Ω, then, there exists a steady-solution $(u_s(x), v_s(x))$ of (6), (7), and

$$\lim_{t\to\infty} \|u(x,t) - u_s(x)\|_{L^2} + \|v(x,t) - v_s(x)\|_{L^2} = 0.$$

(3) *Under condition (11), there is a ball $B = B(f,g,\mu) \subset L^\infty(\Omega)$ such that fro any initial data $\tilde{u}_0, \tilde{v}_0 \in B$, verifying the neccessary compatibility conditions, the corresponding classical solution $(\tilde{u}, \tilde{v})$ converges to the steady-state (u_s, v_s), that*

is

$$\lim_{t\to\infty} \|\tilde{u}(x,t) - u_s(x)\|_{L^2} + \|\tilde{v}(x,t) - v_s(x)\|_{L^2} = 0.$$

In particular, (u_s, v_s) *is asymptotically stable.*

4.2 Proof of main theorem

The proof is given below in a series of lemmas, where (u, v) is a local, classical solution of the problem. We will make a repeated use the of the maximum principle, that can be found, for example, the book by Evans (2010).

Lemma 1 *Let* $w \in C^{1,2}(Q_T) \cap C(\overline{Q_T})$ *be a function that satisfies,*

$$\partial_t w - \mu \Delta w \leq (\geq) - kw,$$

where $\mu, k \geq 0$. *Then,*

$$\max_{Q_T} w(x,t) = \max_{\Gamma_T} w(x,t),$$

or, if the inequality is reversed,

$$\min_{Q_T} w(x,t) = \min_{\Gamma_T} w(x,t).$$

Since $f(x), g(x) \geq 0$, it follows from this lemma that $u(x,t)$ and $v(x,t)$ are non-negative functions. We proceed with uniform upper bounds.

Lemma 2 *There is* $C > 0$, *depending on* a, b, c, d, $\max u_0$, $\max v_0$, $\max f(x)$ *and* $\max g(x)$, *but not* μ, *such that*

$$\begin{aligned} &\max_{(x,t)\in Q_T} u(x,t), \max_{(x,t)\in Q_T} v(x,t) \\ &\quad \leq C\left(\|u_0\|_\infty, \|v_0\|_\infty, \|f\|_\infty, \|g\|_\infty\right), \end{aligned} \tag{12}$$

where C *is polynomial function of its arguments, with positive coefficients, and is independent of* μ.

Proof Let Z be a solution of the ordinary differential equation,

$$\partial_t Z = -aZ - \|f\|_\infty,$$

with initial condition $Z(0) = 0$, i.e., $Z(t) = \left(e^{-at} - 1\right)\frac{\|f\|_\infty}{a}$. Setting $\hat{u}(x,t) = u(x,t) + Z(t)$ we find that

$$\partial_t \hat{u} - \mu \Delta \hat{u} = -a\hat{u} + \frac{b(\hat{u} - Z)^2}{1+v} + f(x) - \|f\|_\infty$$

$$\leq -a\hat{u} + \frac{b(\hat{u} - Z)^2}{1 + v}. \tag{13}$$

As for v, we have,

$$\partial_t v - \mu \Delta v = -cv + d(\hat{u} - Z)^2 + g(x) \geq -cv + d(\hat{u} - Z)^2. \tag{14}$$

Let ϕ be a smooth, non-increasing function that will be chosen later. For function $\phi(v(x,t))$ we obtain

$$\partial_t \phi(v) - \mu \Delta \phi(v) + \mu \phi''(v)|\nabla v|^2 + cv\phi'(v) - d(\hat{u} - Z)^2 \phi'(v) \leq 0.$$

Adding the last equation to (13) we get,

$$\partial_t \big(\hat{u} + \phi(v)\big) - \mu \left(\Delta \hat{u} + \Delta \phi(v)\right) + \phi''(v)|\nabla v|^2 + a\hat{u} + cv\phi'(v) \\ -(\hat{u} - Z)^2 \left(\frac{b}{1 + v} + d\phi'(v)\right) \leq 0.$$

We will select $\phi = -\frac{b}{d} \ln(1 + v)$, so that

$$\partial_t \big(\hat{u} + \phi(v)\big) - \mu \Delta \big(\hat{u} + \phi(v)\big) \leq -a(\hat{u} + \phi(v)) + a\phi(v) + \frac{bc}{d} \frac{v}{1 + v} \\ \leq -a(\hat{u} + \phi(v)) + \alpha \max_{Q_T} \ln(1 + v), \tag{15}$$

for some α depending on a, b, c, d. Let W be a solution of

$$\partial_t W = -aW + \alpha \max_{Q_T} \ln(1 + v),$$

with initial condition $W(0) = 0$, i.e., $W(t) = \alpha_1 \max_{Q_T} \ln(1 + v) \left(1 - e^{-at}\right)$, with $\alpha_1 = \alpha/a$. Subtracting equation for W from (15), we obtain:

$$\partial_t \big(\hat{u} + \phi(v) - W\big) - \mu \Delta \big(\hat{u} + \phi(v) - W\big) \leq -a \left(\hat{u} + \phi(v) - W\right).$$

Now, using the maximum principle (1) we obtain

$$\max_{Q_T} (\hat{u} + \phi - W) = \max \left(\max_{\Omega \times \{0\}} (\hat{u} + \phi), \max_{\Gamma_T} (Z(t) + \phi(v) - W(t)) \right) \\ \leq \max \left(\max_{\Gamma_T} u_b, \max_{\Omega} (u_0 + Z(0) + \phi_0) \right) \leq \max_{\Omega} u_0.$$

Therefore, for any (x,t) in the domain Q_T, $\hat{u} + \phi - W \leq \max_{\Omega} u_0$, or,

$$\hat{u}(x,t) \leq \frac{b}{d} \ln(1 + v(x,t)) + W(t) \leq \max_{\Omega} u_0 + \alpha_2 \ln(1 + \max_{Q_T} v), \tag{16}$$

for some α_2 depending on a, b, c, d.

Consider now Eq. (14).

$$\partial_t v - \mu \Delta v = -cv + d(\hat{u} - Z)^2 + g(x)$$
$$\leq -cv + d\left(\max_{\Omega} u_0 + \alpha_2 \ln(1 + \max_{Q_T} v) + \frac{\|f\|_\infty}{a}\right)^2 + \|g\|_\infty.$$

Using a maximum principle again we get

$$\max_{Q_T} v \leq \max_{\Omega} v_0 + \frac{d}{a}\left(\max_{\Omega} u_0 + \alpha_2 \ln(1 + \max_{Q_T} v) + \frac{\|f\|_\infty}{a}\right)^2 + \frac{1}{a}\|g\|_\infty.$$

By the elementary properties of function $\ln(1+v)$, we find that $\max_{Q_T} v$ is bounded by a polynomial with positive coefficients in variables of $\max u_0$, $\max v_0$, $\|f\|_\infty$, $\|g\|_\infty$. The corresponding estimate for $\max_{Q_T} u$ follows from this and (16). □

Now, the global existence follows.

Lemma 3 *The unique, local, classical solution (u, v) can be extended for all times $t > 0$.*

Proof We will use the following characterization of maximal time of existence T of a local solution, from Rothe (1984), theorem 1, page 111. It is proved there that if $T < +\infty$ then the max–norm over x of $(u(x,t), v(x,t))$ grows without bound as t approaches T. But this can not happen due to the estimates derived above in (12). Therefore, the contradiction leads us to conclude that the classical solution in fact exists for all times $t > 0$. □

To show that the classical solution (u, v) of the reaction-diffusion system settles on a steady state it sufficient to show that the time derivative of the solution converges to zero. We will use an energy-type estimate to establish this fact. The proof makes use of the Poincare's inequality that we state for a reference below.

Lemma 4 *Let Ω be a bounded, connected, open subset of $\mathbb{R}^n$ with a C^1 boundary $\partial\Omega$. Let $1 \leq p < \infty$. Then there exists a constant C, depending only on n, p and Ω, such that for any integrable function u with $\nabla u \in L^p(\Omega)$ and zero trace on the boundary $\partial\Omega$,*

$$\|u\|_{L^p(\Omega)} \leq C(\Omega, p)\|\nabla u\|_{L^p(\Omega)}. \tag{17}$$

Proof can be found in Brezis book Brezis (2001).

Lemma 5 *For all $t \in [0, T]$, $T > 0$, it holds:*

$$\frac{d}{dt}\left(\|u_t\|_2^2 + \|v_t\|_2^2\right) + 4(\mu C(\Omega) - C_s)\left(\|u_t\|_2^2 + \|v_t\|_2^2\right) \leq 0,$$

where $C_s = C_s(\max_{Q_T} u, \max_{Q_T} v)$ is a polynomial function of its arguments, and is independent of μ, and T, and $C(\Omega)$ is the reciprocal of constant $C(\Omega, 2)$ from the Poincare's inequality. If the stability condition

$$C_s < \mu C(\Omega) \tag{18}$$

holds, then

$$\|u_t(x,t)\|_2^2 + \|v_t(x,t)\|_2^2 \leq e^{-4(\mu C(\Omega) - C_s)t} \left(\|u_0\|_{C^2(\Omega)}^2 + \|v_0\|_{C^2(\Omega)}^2 \right) \to 0,$$

as $t \to +\infty$.

Proof Taking time derivative of both sides of the equation for u (1), we get,

$$\partial_t u_t - \mu \Delta u_t = -a u_t + 2b \frac{u\, u_t}{(1+v)} - b \frac{u^2\, v_t}{(1+v)^2}.$$

Multiply with u_t and integrate over the domain to get,

$$\int_\Omega u_t \partial_t u_t \, dx - \mu \int_\Omega u_t \Delta u_t \, dx = -a \int_\Omega |u_t|^2 \, dx + 2b \int_\Omega \frac{u\,|u_t|^2}{(1+v)} \, dx - b \int_\Omega \frac{u^2\, u_t\, v_t}{(1+v)^2} \, dx.$$

Using integration by parts,

$$\frac{1}{2}\frac{d}{dt} \int_\Omega |u_t|^2 \, dx - \mu \int_\Gamma u_t \nabla u_t \cdot n \, d\sigma + \mu \int_\Omega |\nabla u_t|^2 \, dx = -a \int_\Omega |u_t|^2 \, dx + 2b \int_\Omega \frac{u\,|u_t|^2}{(1+v)} \, dx - b \int_\Omega \frac{u^2\, u_t\, v_t}{(1+v)^2} \, dx.$$

We will use Young's inequatlity, uniform bounds on u and v, and Poincaré's inequality (17) with $p = 2$ applied to the function $\partial_t u$ (notice, that $\partial_t u$ equals to zero on the boundary of the domain) to get the next result. The constant $C(\Omega, 2)^{-1}$ from that inequality will be abbreviated to $C(\Omega)$.

$$\frac{1}{2}\frac{d}{dt} \int_\Omega |u_t|^2 \, dx \leq (-\mu\, C(\Omega) + c_0) \int_\Omega |u_t|^2 + |v_t|^2 \, dx, \tag{19}$$

where c_0 has polynomial dependence on $\max u$, $\max v$. Similarly, for v,

$$\frac{1}{2}\frac{d}{dt} \int_\Omega |v_t|^2 \, dx \leq (-\mu\, C(\Omega) + c_0) \int_\Omega |u_t|^2 + |v_t|^2 \, dx.$$

$$\frac{1}{2}\frac{d}{dt} \int_\Omega |u_t|^2 + |v_t|^2 \, dx \leq 2\,(-\mu\, C(\Omega) + c_0) \int_\Omega |u_t|^2 + |v_t|^2 \, dx. \tag{20}$$

Now the statement of the lemma follows from the last inequality and uniform bounds from lemma 2 □

When uniform estimates from lemma 2 are substituted into function C_s in lemma 5, condition (18) defines the range of L^∞ norms of admissible data $\|f\|_\infty$, $\|g\|_\infty$, $\|u_0\|_\infty$, $\|v_0\|_\infty$. We can state this in another way, by saying that if f and g are such that stability condition (11) holds with $u_0 = 0$ and $v_0 = 0$, then there is a ball $B = B(f, g, \mu) \subset L^\infty(\Omega)$, centered at zero such that the same condition (11) holds for any $u_0, v_0 \in B$. In the remaining part of the proof we will assume this condition.

Next we will obtain bound on the gradients of ∇u, ∇v.

Lemma 6 *For any $t > 0$,*

$$\mu \int_\Omega \left(|\nabla u(x,t)|^2 + |\nabla v(x,t)|^2 \right) dx \le C(\|f\|_\infty, \|g\|_\infty, \|u_0\|_{C^2}, \|v_0\|_{C^2}),$$

with a positive C, independent of time.

Proof We multiply for u by u_t and integrate by parts to get,

$$\begin{aligned} &\int_\Omega |u_t|^2 \, dx - \mu \int_\Gamma u_t \nabla u \cdot n \, d\sigma \\ &+\mu \int_\Omega \nabla u \cdot \nabla u_t \, dx = -a \int_\Omega u u_t \, dx \\ &+b \int_\Omega \frac{u^2}{1+v} u_t \, dx + \int_\Omega f(x) u_t \, dx. \end{aligned}$$

Using boundary condition on u_t and uniform bounds on u and v from lemma 2,

$$\begin{aligned} &\int_\Omega |u_t|^2 \, dx + \mu \frac{1}{2} \frac{d}{dt} \int_\Omega |\nabla u|^2 \, dx \\ &= -a \int_\Omega u u_t \, dx + b \int_\Omega \frac{u^2}{1+v} u_t \, dx + \int_\Omega f(x) u_t \, dx \\ &\le (c_0 + \|f\|_\infty) \int_\Omega |u_t| \, dx = c_1 \|u_t\|_2, \end{aligned}$$

with an appropriate c_0. Similarly, for v, we get,

$$\int_\Omega |v_t|^2 \, dx + \mu \frac{1}{2} \frac{d}{dt} \int_\Omega |\nabla v|^2 \, dx \le c_1 \|v_t\|_2.$$

Adding the last two inequalities we get,

$$\mu \frac{d}{dt} \int_\Omega \left(|\nabla u|^2 + |\nabla v|^2 \right) dx \le c_1 \left(\|u_t\|_2 + \|v_t\|_2 \right).$$

We integrate this inequality in time from 0 to t, use exponential decay estimate on $\|u_t\|_2$, $\|v_t\|_2$ from previous lemma, together with uniform bounds on u and v to get:

$$\begin{aligned}
&\mu \int_\Omega \left(|\nabla u(x,t)|^2 + |\nabla v(x,t)|^2 \right) dx \\
&\leq \mu \int_\Omega \left(|\nabla u_0|^2 + |\nabla v_0|^2 \right) dx \\
&+ c_1 \int_0^t \left(\|u_t\|_2 + \|v_t\|_2 \right) dt \leq C,
\end{aligned}$$

with some $C > 0$, as stated in the lemma. □

Let $u(x,t)$, $v(x,t)$ be the solution from the previous section. Let t_n be a non-decreasing sequence of time converging to $+\infty$. Consider sequences of functions $\{u_n(x) = u(x,t_n)\}$ and $\{v_n(x) = v(x,t_n)\}$. From the estimates of u, v and their gradients, it holds that there is C independent of n such that

$$\begin{aligned}
&\|u_n\|_2 \leq C, \quad \|v_n\|_2 \leq C, \\
&\|\nabla u_n\|_2 \leq C, \quad \|\nabla v_n\|_2 \leq C.
\end{aligned}$$

We will need the following compactness result, the proof of which can be found in chapter 5 of Evans book Evans (2010).

Lemma 7 *Assume Ω is a bounded open subset of $\mathbb{R}^n$, and $\partial\Omega$ is C^1. Suppose $1 \leq p < n$. Then, there is a compact embedding*

$$W^{1,p}(\Omega) \subset\subset L^q(\Omega), \tag{21}$$

for each $1 \leq q < \frac{np}{n-p}$.

Since Ω is a bounded set it follows this theorem that both sequences are pre-compact in $L^2(\Omega)$. This means that there is a subsequence of $\{t_n\}$, that we still label by n, and two functions $u, v \in W^{1,2}(\Omega)$ such that

$$\lim_{n\to\infty} u_n = u_s, \quad \lim_{n\to\infty} v_n = v_s$$

in L^2 norm. From the convergence in norm, it follows that a further subsequence can be extracted such that u_n and v_n converge to u_s and v_s almost everywhere in Ω. Moreover, since $L^2(\Omega)$ is a reflexive space and ∇u_n, ∇v_n are from bounded sets, there is still further subsequence such that

$$\nabla u_n \to \nabla u_s, \quad \nabla v_n \to \nabla v_s,$$

weakly in $L^2(\Omega)$.

Moreover, from Lemma 5 it follows that

$$u_t(x,t_n) \to 0, \quad v_t(x,t_n) \to 0$$

in L^2 norm.

Now we pass to the limit in the equations.

Lemma 8 *The limiting pair of functions (u_s, v_s) is a classical solution of the system of equations:*

$$-\mu\Delta u_s = -au_s + \frac{bu_s^2}{1+v_s} + f,$$
$$-\mu\Delta v_s = -cv_s + dv_s^2 + g.$$

Proof Let $\omega(x)$ be a smooth test function, equal to zero on the boundary $\partial\Omega$. From the original reaction-diffusion system, considered at times $t = t_n$ we obtain the following integral relations:

$$\int u_t(x,t_n)\omega(x)\,dx + \mu\int \nabla u_n\cdot\nabla\omega(x)\,dx$$
$$= \int\left(-au_n + \frac{bu_n^2}{1+v_n} + f(x)\right)\omega(x)\,dx,$$
$$\int v_t(x,t_n)\omega(x)\,dx + \mu\int \nabla v_n\cdot\nabla\omega(x)\,dx = \int\left(-cv_n + dv_n^2 + g(x)\right)\omega(x)\,dx.$$

Passing to the limit in each term of these equations, using above compactness properties we obtain that

$$\mu\int \nabla u_s\cdot\nabla\omega\,dx = \int\left(-au_s + \frac{bu_s^2}{1+v_s} + f\right)\omega\,dx,$$
$$\mu\int \nabla v_s\cdot\nabla\omega\,dx = \int\left(-cv_s + dv_s^2 + g\right)\omega\,dx.$$

i.e, (u_s, v_s) is a weak solution. As a pointwise limit of $u(x,t_n)$, $v(x,t_n)$, (u_s, v_s) take boundary values u_b and v_b. By the well know regularity results for elliptic equations, it follows that $u_s, v_s \in C^{2+\alpha}(\overline{\Omega})$, and it is classical solutions of the same system. □

Now we prove the following.

Lemma 9 *As $t\to\infty$, $u(x,t)$, $v(x,t)$ of the system converges to $u_s(x)$, $v_s(x)$ in L_2 norm:*

$$\lim_{t\to\infty}\|u(x,t) - u_s(x)\|_2 = 0, \quad \lim_{t\to\infty}\|v(x,t) - v_s(x)\|_2 = 0.$$

Proof Suppose that $(u(x,t), v(x,t))$ does not converge to (u_s, v_s) in L^2 norm. Then, there is a sequence of times t_n and $\epsilon > 0$ such that

$$\|(u(x,t_n), v(x,t_n)) - (u_s(x), v_s(x))\|_2 \geq \epsilon.$$

Using the arguments of this section we conclude that there is another steady-state $(\tilde{u}_s, \tilde{v}_s)$ and

$$\|(\tilde{u}_s, \tilde{v}_s) - (u_s(x), v_s(x))\|_2 \geq \epsilon. \tag{22}$$

Since (u_s, v_s) and $(\tilde{u}_s, \tilde{v}_s)$ solve the same system of equations, subtraction corresponding equations, multiplying them by $\tilde{u}_s - u_s$ and $\tilde{v}_s - v_s$, and integrating over Ω, after simple manipulations we get

$$(\mu C(\Omega) - C_s) \int |\tilde{u}_s - u_s|^2 + |\tilde{v}_s - v_s|^2 \, dx \leq 0,$$

where C_s and $C(\Omega)$ as in (18). Since $\mu C(\Omega) - C_s$ is positive, we conclude that $\tilde{u}_s = u_s$ and $\tilde{v}_s = v_s$. This clearly contradicts statement (22) and the lemma is proved. □

In the next theorem we show that the steady state (u_s, v_s) is asymptotically stable.

Lemma 10 *Let (u, v) be a classical solution of the reaction-diffusion system (6), (7) with initial data u_0, v_0 in $B(f, g, \mu) \cap C^{2+\alpha}$ and boundary conditions (8). Then, for any $t > 0$,*

$$\|(u(x,t) - u_s(x), v(x,t) - v_s(x))\|_2 \leq e^{-Kt} \|(u_0(x) - u_s(x), v_0(x) - v_s(x))\|_2, \tag{23}$$

where $K = 4(\mu C(\Omega) - C_s)$.

Proof Let $(U, V) = (u - u_s, v - v_s)$. Subtracting corresponding equation for (u, v) and (u_s, v_s) we get,

$$\begin{aligned} \partial_t U - \mu \Delta U &= -aU + b\left(\frac{u^2}{1+v} - \frac{u_s^2}{1+v_s}\right), \\ \partial_t V - \mu \Delta V &= -cV + d\left(u^2 - u_s^2\right). \end{aligned}$$

As in the proof of lemma 4 we obtain

$$\frac{1}{2}\frac{d}{dt} \int |U|^2 + |V|^2 \, dx + 2(\mu C(\Omega) - C_s) \int |U|^2 + |V|^2 \, dx \leq 0.$$

Using Gronwall's inequality, we get that,

$$\int |U(x,t)|^2 + |V(x,t)|^2 \, dx \leq e^{-Kt} \int |U_0(x)|^2 + |V_0(x)|^2 \, dx.$$

where $K = 4(\mu C(\Omega) - C_s) > 0$. The statement of the lemma follows from this. □

5 Conclusions

In this paper we address the mathematical modeling of recent experimental studies on self-organization of human embryonic stem cells during early stages embryo's development. Although several models based on reaction-diffusion equations were proposed in literature, those results are only partially satisfactory as they either contain a number of artificial assumptions on the reaction part of the model or use initial and boundary conditions that do not correspond to the experimental setup.

We showed that an Gierer-Meinhardt system of reaction-diffusion equations, with properly selected reaction coefficients and supplemented with Robin-type boundary conditions, qualitatively reproduces many of the experimental findings, thus identifying a proper mathematical framework. In this paper we only present numerical results for circular domains for brevity of presentation. Additional experiments with domains of irregular shapes, including non-convex domains, were presented by Bedekar Bedekar (2020). All numerical simulations confirm very good qualitative agreement between our models and in vitro experiments. Moreover, the model produces various new phenomena for the reaction-diffusion system under investigation such as an interesting instability investigated numerically in Sect. 3.4.

The second part of the paper is motivated by the numerical results obtained in the first part, and addresses the existence of of non-homogeneous steady state solutions that asymptotically attract solutions of the reactions-diffusion system. In general, this is a hard mathematical problem, which we were able to address under certain simplifying assumptions about the system.

With proper ramifications, the model considered in this paper can potentially lead to important scientific insights into the behavior of the biological system. In particular, instabilities outlined in numerical experiments performed here warrant careful analytical investigation. In addition, we can use experimental data to estimate parameters in the PDE model via a Bayesian approach and use the resulting realistic model to predict outcomes of experiments in domains of various sizes. We intend to carry out further investigation of the reaction-diffusion model presented here in subsequent papers.

Acknowledgements The authors would like to thank the anonymous reviewers for providing many valuable comments on the paper that helped to improve it in many ways.

6 Appendix

We use the following activator-inhibitor system for the dynamics of BMP/Nogin:

$$\begin{aligned} \partial_t u - \mu_{bmp}\Delta u &= -\lambda_{bmp} u + k_{bmp}\frac{u^2}{\tilde{v}+v}, \\ \partial_t v - \mu_{nog}\Delta v &= -\lambda_{nog} v + \frac{k_{nog}}{\tilde{u}}u^2, \end{aligned}$$

where $\tilde{u}$, $\tilde{v}$ are some reference values for BMP4 and Noggin. The boundary conditions are

Table 2 Values for the diffusion and reaction parameters

Parameters	Values	SI units
μ_{bmp}	11	$\mu m^2/sec$
μ_{nog}	55	$\mu m^2/sec$
λ_{bmp}	9×10^{-4}	$1/sec$
k_{bmp}	9×10^{-4}	$1/sec$
λ_{nog}	9×10^{-4}	$1/sec$
k_{nog}	9×10^{-4}	$1/sec$

$$\frac{\partial u}{\partial n} = H_{bmp}\,(\bar{u} - u)\,, \quad \frac{\partial v}{\partial n} = -\,H_{nog} v.$$

where $\bar{u}$ is the background value of BMP4, and H_{bmp}, H_{nog} are positive numbers. The initial conditions: $u(x, 0) = \bar{b}$, $v(x, 0) = 0$, which correspond to a cell colony being treated with high concentration of BMP4. The typical magnitudes of the parameters are listed in Table 2.

The colony size (radius of the disk) $L = 500\,\mu m$, and a typical experiment takes up to 3 days (3τ, $\tau = 86400 sec$). The experimental data on the values of H_{bmp} and H_{nog} are not available. We set them to 1 $(\mu m)^{-1}$.

Scaling the variables: $x \to Lx$, $t \to \tau t$, $u \to \tilde{u}u$, $v \to \tilde{v}v$, with $\tilde{u}/\tilde{v} = 1$, we obtain a system with non-dimensionless coefficients:

$$\begin{aligned}
\partial_t u - \frac{\mu_{bmp}\tau}{L^2}\Delta u &= -\,(\lambda_{bmp}\tau)u + (k_{bmp}\tau)\frac{u^2}{1+v}, \\
\partial_t v - \frac{\mu_{nog}\tau}{L^2}\Delta v &= -\,(\lambda_{nog})\tau v + (k_{nog}\tau)u^2,
\end{aligned}$$

with the boundary conditions

$$\frac{\partial u}{\partial n} = H_{bmp} L\left(\frac{\bar{u}}{\tilde{u}} - u\right), \quad \frac{\partial v}{\partial n} = -\,H_{nog} L v.$$

This leads to the system (1), (2) with coefficients $h_u = H_{bmp}L$, $h_v = H_{nog}L$, $\mu_u = \mu_{bmp}\tau L^{-2}$, $\mu_v = \mu_{nog}\tau L^{-2}$, $a = \lambda_{bmp}\tau$, $b = k_{bmp}\tau$, $c = \lambda_{nog}\tau$, $d = k_{nog}\tau$, the values of which are listed in Table 1. For the boundary and initial conditions, ratio $\bar{u}/\tilde{u} = 3$. The scaling for Wnt/DKK and Nodal/Lefty RD systems are similar.

The numerical simulations are based on the forward Euler approximation of time derivatives combined with a finite element method, using piece-wise linear functions for the space discretization, and a suitable triangulation of the domain. Space and time partitions steps, (h, δ) were set to $h = 10^{-3}$ and $\delta = 10^{-6}$, with $\delta = h^2$, to prevent numerical instabilities. The method was implemented using FreeFem++, see Hecht (2012).

References

Arnold SJ, Robertson EJ (2009) Making a commitment: cell lineage allocation and axis patterning in the early mouse embryo. Nat Rev Mol Cell Biol 10:91–103. https://doi.org/10.1038/nrm2618 (**PMID: 19129791**)

Brezis H (2001) Functional analysis. Sobolev spaces and partial differential equations. Springer, New York

Bedekar P (2020) Mathematical Models of Self-Organized Patterning of human Embryonic Stem Cells (hESCs), University of Houston Ph.D. thesis, Department of Mathematics

Brinkmann F, Mercker M, Richter T, Marciniak-Czochra A (2018) Post-turing tissue pattern formation: advent of mechanochemistry. PLOS Comput Biol 14(7):e1006259

Chhabra S, Liu L, Goh R, Kong X, Warmflash A (2019) Dissecting the dynamics of signaling events in the BMP, WNT, and NODAL cascade during self-organized fate patterning in human gastruloids. PLoS Biol 17(10):e3000498

Chueh K, Conley C, Smoller J (1977) Positively invariant regions for systems of nonlinear diffusion equations. Ind U Math J 26:373–392

Crampin E, Gaffney E, Maini P (1999) Reaction and diffusion on growing domains: scenarios for robust pattern formation. Bull Math Biol 61:1093–1120

Evans LC (2010) Partial differential equations. Graduate studies in mathematics. AMS, Providence

Etoc F et al (2016) A Balance between secreted inhibitors and edge sensing controls gastruloid self-organization. Dev Cell 39:302–315

Fu J, Warmflash A, Lutolf MP (2021) Stem-cell-based embryo models for fundamental research and translation. Nat Mater 20:132–144

Heemskerk I, Burt K, Miller M, Chhabra S, Cecilia Guerra M, Liu L (2019) Rapid changes in morphogen concentration control self-organized patterning in human embryonic stem cells. Elife 8:e40526. https://doi.org/10.7554/eLife.40526.001

Maini PK, Baker RE, Chuong CM (2006) Developmental biology. The Turing model comes of molecular age. Science 314(5804):1397–8. https://doi.org/10.1126/science.1136396

Gierer A, Meinhardt H (1972) A theory of biological pattern formation. Kybernetik 12(1):30–9. https://doi.org/10.1007/BF00289234

Glover JD, Wells KL, Matthäus F, Painter KJ, Ho W et al (2017) Hierarchical patterning modes orchestrate hair follicle morphogenesis. PLOS Biol 15(7):e2002117. https://doi.org/10.1371/journal.pbio.2002117

Hecht F (2012) New development in FreeFem++. J Numer Math 20(3–4):251–266

Hillen T, Painter KJ (2009) A user's guide to PDE models for chemotaxis. J. Math. Biol. 58:183. https://doi.org/10.1007/s00285-008-0201-3

Koch AJ, Meinhardt H (1994) Biological pattern formation: form basic mechanisms to complex structures. Rev Mod Phys 66(4):1481–508

Krause AL, Klika V, Halatek J et al (2020) Turing patterning in stratified domains. Bull Math Biol 82:136

Ladyzenskaja OA, Solonnikov VA, Ural'ceva NN (1995) Linear and Quasi-linear Equations of Parabolic Type. Translations of mathematical monographs series. AMS: Providence

Liu L, Warmflash A (2021) Self-organized signaling in stem cell models of embryos. Stem cell reports 16:1065–1077

Mercker M, Hartmann D, Marciniak-Czochra A (2013) A mechanochemical model for embryonic pattern formation: coupling tissue mechanics and morphogen expression. PLoS One 8(12):e82617

Muncie JM et al (2020) Mechanical tension promotes formation of gastrulation-like nodes and patterns mesoderm specification in human embryonic stem cells. Dev Cell 55:679–694.e11

Murray JD (1989) Mathematical biology. Springer-Verlag, Berlin

Murray JD, Oster GF, Harris AK (1983) A mechanical model for mesenchymal morphogenesis. J Math Biol 17:125–129

Raspopovic J, Marcon L, Russo L, Sharpe J (2014) Digit patterning is controlled by a Bmp-Sox9-Wnt Turing network modulated by morphogen gradients. Science 345(6196):566–70. https://doi.org/10.1126/science.1252960PMID25082703

Nakamura T, Mine N, Nakaguchi E, Mochizuki A, Yamamoto M, Yashiro K (2006) Generation of robust left-right asymmetry in the mouse embryo requires a self-enhancement and lateral-inhibition system. Dev Cell 11(4):495–504. https://doi.org/10.1016/j.devcel.2006.08.002 (**PMID: 17011489**)

Rothe F (1984) Global solutions of reaction-diffusion systems. Springer-Verlag, Berlin

Smoller J (1983) Shock waves and reaction-diffusion equations. Springer-Verlag, New- York

Tewary M, Ostblom J, Prochazka L, Zulueta-Coarasa T, Shakiba N, Fernandez-Gonzalez R, Zandstra PW (2017) A stepwise model of reaction-diffusion and positional information governs self-organized human peri-gastrulation-like patterning. Development 144(23):4298–4312. https://doi.org/10.1242/dev.149658

Turing AM (1952) The chemical basis of morphogenesis. Philos Trans R Soc B Biol Sci 237(641):37–72. https://doi.org/10.1098/rstb.1952.0012

Van Gorder RA, Klika V, Krause AL (2021) Turing conditions for pattern forming systems on evolving manifolds. J Math Biol 82:4. https://doi.org/10.1007/s00285-021-01552-y

Warmflash A, Sorre B, Etoc F, Siggia ED, Brivanlou AH (2014) A method to recapitulate early embryonic spatial patterning in human embryonic stem cells. Nat Methods 11(8):847–54. https://doi.org/10.1038/nmeth.3016 (**PMID: 24973948**)